

# Orientation microscopy–assisted grain boundary analysis for protonic ceramic cell electrolytes

Sooraj Patel<sup>1</sup>  | Sumit Goswami<sup>2</sup> | Pralay Paul<sup>2</sup> | Fan Liu<sup>3,4</sup> |  
Shuanglin Zheng<sup>1</sup> | Julian E. Sabisch<sup>5</sup> | Chuancheng Duan<sup>3,6</sup> |  
Thirumalai Venkatesan<sup>2</sup> | Hanjong Paik<sup>2,7</sup> | Hanping Ding<sup>1</sup> |  
Pejman Kazempoor<sup>1</sup> | Shuzhi Xu<sup>1</sup> | Dong Ding<sup>4</sup> | Iman Ghamarian<sup>1</sup>

<sup>1</sup>School of Aerospace and Mechanical Engineering, The University of Oklahoma, Norman, Oklahoma, USA

<sup>2</sup>Center for Quantum Research and Technology, The University of Oklahoma, Norman, Oklahoma, USA

<sup>3</sup>Department of Chemical Engineering, Kansas State University, Manhattan, Kansas, USA

<sup>4</sup>Energy & Environmental Science and Technology, Idaho National Laboratory, Idaho Falls, Idaho, USA

<sup>5</sup>Samuel Roberts Noble Microscopy Laboratory, The University of Oklahoma, Norman, Oklahoma, USA

<sup>6</sup>Department of Chemical Engineering, University of Utah, Salt Lake City, Utah, USA

<sup>7</sup>School of Electrical and Computer Engineering, The University of Oklahoma, Norman, Oklahoma, USA

## Correspondence

Iman Ghamarian, School of Aerospace and Mechanical Engineering, The University of Oklahoma, Norman, OK, USA.

Email: [iman@ou.edu](mailto:iman@ou.edu)

## Funding information

Research Council of the University of Oklahoma; HydroGEN Advanced Water Splitting Materials Consortium, the U.S. Department of Energy (USDOE); Office of Energy Efficiency and Renewable Energy; Hydrogen and Fuel Cell Technologies Office, Grant/Award Number: DE-AC07-05ID14517

## Abstract

Grain boundaries in protonic ceramic cell (PCC) electrolytes hinder proton transport, reducing interfacial conductivity. In multicomponent PCC electrolytes, the inclusion of sintering aids further accentuates the complexity of grain boundaries. In this study, we synthesize nanocrystalline  $\text{BaCe}_{0.4}\text{Zr}_{0.4}\text{Y}_{0.1}\text{Yb}_{0.1}\text{O}_{3-\delta}$  thin films via pulsed laser deposition and analyze their grain boundary character distributions using orientation data collected by precession electron diffraction technique. The results reveal an anisotropic distribution of grain boundary characters, with notably high populations of  $180^\circ$ -tilt and twist grain boundaries. These findings provide critical insights into identifying the predominant grain boundaries in this PCC electrolyte material, assessing the vast five-dimensional grain boundary space.

## KEY WORDS

grain boundary character distribution, precession electron diffraction, protonic conductor, pulsed laser deposition, transmission electron microscopy

## 1 | INTRODUCTION

Protonic ceramic cells (PCCs) have emerged as promising alternatives to traditional oxygen-ion-conducting solid oxide cells, primarily due to protons' lower migration energy barrier relative to oxygen ions.<sup>1–3</sup> This reduced activation energy enables efficient operation

of PCCs at temperatures even below  $450^\circ\text{C}$ , making them attractive for power generation and green hydrogen production.<sup>4</sup> To minimize ionic resistance, achieving optimal performance in PCC electrolytes requires high ionic conductivity, negligible electronic conductivity, and thin-film architectures.<sup>5,6</sup> Perovskite oxides, particularly  $\text{Ba}(\text{Ce},\text{Zr})\text{O}_3$  systems doped with Y and

Yb, have demonstrated promise as PCC electrolytes. Among these,  $\text{BaCe}_{0.4}\text{Zr}_{0.4}\text{Y}_{0.1}\text{Yb}_{0.1}\text{O}_{3-\delta}$  (BCZYYb4411) has received growing attention due to its enhanced steam tolerance and electrochemical performance, making it a promising candidate for proton-conducting electrolytes in hydrogen production applications.<sup>7–9</sup>

Fabricating ultrathin electrolytes reduces ohmic resistance and facilitates efficient proton transport. Recent advancements in pulsed laser deposition (PLD) have enabled the formation of thin, dense, and uniform PCC films with improved properties.<sup>10–12</sup> For instance, Bae et al.<sup>13</sup> achieved an open-circuit voltage of 1.0 V and a remarkable power density of 740 mW cm<sup>-2</sup> using a PLD-prepared  $\text{BaZr}_{0.85}\text{Y}_{0.15}\text{O}_{3-\delta}$  PCC electrolyte. Both bulk and grain boundary contributions influence proton conductivity in these electrolytes; however, grain boundaries typically exhibit higher resistance than the bulk,<sup>14,15</sup> especially at lower operating temperatures, making them critical to overall proton transport. Factors such as dopant segregation, space-charge layers, and local structural distortions can all contribute to reduced grain boundary conductivity.<sup>16–18</sup> Grain boundary geometries significantly influence grain growth dynamics<sup>19,20</sup> and the segregation of solute atoms or impurities.<sup>21–23</sup> Consequently, unraveling the complexity of grain boundaries and their character distributions is essential for optimizing PCC electrolyte performance.

Macroscopic characterization of grain boundary geometry involves analyzing the misorientations between grains and the distribution of grain boundary planes.<sup>24</sup> Misorientation data for individual grain boundaries can be obtained from orientation maps, whereas grain boundary plane data can be reconstructed through three-dimensional mapping from a series of two-dimensional orientation datasets<sup>25</sup> or estimated using stereological approaches.<sup>26</sup> Grain boundary misorientations are characterized by three parameters, typically represented by Bunge Euler angles ( $\phi_1, \Phi, \phi_2$ ), where  $\phi_1$  and  $\phi_2$  range from 0 to  $\frac{\pi}{2}$ , and  $\cos\Phi$  ranges from 0 to 1. In the crystal reference frame, two additional parameters ( $\theta$  and  $\varphi$ ) define the orientation of the grain boundary plane normal, with  $\cos(\theta)$  ranging from 0 to 1 and  $\varphi$  from 0 to  $2\pi$ .<sup>27</sup> The five-parameter grain boundary character space is discretized into bins of equal volume (e.g., 10° for each parameter), and each grain boundary is classified into one of these bins based on its misorientation and grain boundary plane normal.<sup>27</sup> Quantitative analysis of the grain boundary plane distribution is often represented in stereographic plots, where the frequency of occurrence (or relative area) compared to a random distribution is expressed as multiples of random distribution (MRD).

Grain boundary character distribution (GBCD) has been extensively studied in various materials, including base

metals like Al,<sup>28</sup> Zr,<sup>29</sup> and Ti,<sup>30</sup> as well as compounds such as MgO,<sup>27</sup>  $\text{MgAl}_2\text{O}_4$ ,<sup>31</sup> and  $\text{SrTiO}_3$ .<sup>32</sup> Recent studies have extended to oxygen-ion-conducting electrolytes, with five-parameter GBCD and grain boundary energy analyses performed on materials like yttria-stabilized zirconia (YSZ).<sup>25,33</sup> However, a critical gap remains in the grain boundary characterization of PCC electrolyte materials. In multicomponent PCC electrolytes incorporating dopants and sintering aids, these additives can preferentially segregate at grain boundaries, reducing their excess energy. For instance, the segregation of yttrium (dopant)<sup>34,35</sup> and NiO (sintering aid)<sup>35</sup> at grain boundaries is expected to alter the local grain boundary energy, potentially impacting the overall grain boundary distribution. Consequently, a detailed assessment of grain boundary geometries in PCC electrolyte materials is essential for advancing grain boundary engineering strategies. In this work, we address this gap by investigating the five-parameter GBCD in a nanocrystalline BCZYYb4411 thin film electrolyte. By combining PLD synthesis and precession electron diffraction (PED)-based orientation mapping, we quantitatively describe the distribution of grain boundaries along the preferred misorientation axes and angles.

## 2 | EXPERIMENTAL APPROACHES

### 2.1 | Powder synthesis and sample preparation

BCZYYb4411 was synthesized using the conventional solid-state sintering method. Stoichiometric quantities of  $\text{BaCO}_3$ ,  $\text{CeO}_2$ ,  $\text{ZrO}_2$ ,  $\text{Y}_2\text{O}_3$ ,  $\text{Yb}_2\text{O}_3$ , and NiO were accurately weighed and subjected to ball milling in ethanol for 48 h at a rotational speed of approximately 350 rpm. YSZ beads (10 mm diameter) were utilized as the milling medium. The mixture contained 1 wt.% NiO, relative to the total mass of the crystallized BCZYYb4411, serving as a sintering aid to enhance densification. Following milling, the slurry was dried at 120°C for 24 h to obtain a fine powder. The resulting powder was then calcined at 1350°C for 5 h to facilitate phase formation.

BCZYYb thin film was deposited using a Neocera PLD system from a compact BCZYYb target. The target was formed by compressing 10 g of pure-phase BCZYYb powder, followed by sintering at 1450°C for 5 h. A transmission electron microscopy (TEM) grid purchased from Electron Microscopy Sciences with 20 nm  $\text{SiO}_2$  windows served as the substrate, and deposition was conducted at a radiative heater temperature of 800°C in a 50 mTorr oxygen environment. The target-to-substrate distance was maintained at 50 mm. A 248 nm excimer laser with 3.4 J/cm<sup>2</sup> fluence

and 5 Hz frequency was employed for material ablation. Post-deposition, the films were annealed for 1 h at the same temperature and pressure and then cooled at 10°C/min to room temperature.

## 2.2 | Characterization

The crystal structure of BCZYYb4411 was confirmed through x-ray diffraction (XRD) analysis at room temperature, using a step size of 0.02°. Following the sintering of the PLD target, its density and elemental composition were analyzed using scanning electron microscopy and energy-dispersive spectroscopy (EDS). An acceleration voltage of 30 kV and a current of 6 nA were used to achieve a high count rate of approximately 25 000 counts per second.

The crystal structure of the BCZYYb4411 film deposited on the SiO<sub>2</sub> TEM window grid was initially investigated using a JEOL JEM-2010F equipped with an AMT NanoSprint-15 camera using TEM imaging mode. Nanocrystalline grains were observed via bright-field TEM imaging, and the atomic structure was verified by indexing selected area electron diffraction (SAED) patterns generated by the polycrystalline nano-grains. Orientation microscopy was conducted on a JEOL JEM-2800 TEM equipped with a NanoMegas PED system. The electron beam was precessed at 0.3° to improve indexing accuracy by rocking the Ewald sphere in diffraction space, enhancing the signal-to-noise ratio, and suppressing forbidden reflections.<sup>36</sup>

Grain boundary characterization within the nanocrystalline grains was performed through a series of steps. First, precession-based electron diffraction images were acquired for each crystal of interest. To create a comprehensive orientation map, diffraction patterns were recorded across a scanning area of 1.6 μm × 1.6 μm, using a step size of 5 nm. Next, the diffraction patterns were indexed against simulated diffraction patterns using the automated crystal orientation mapping package. This indexing was based on lattice parameters determined through XRD analysis. Each diffraction pattern within the dataset was assigned to a set of Bunge Euler angles, generating an orientation file for the entire scanned area. Subsequently, the raw data were processed using TSL OIM software to reconstruct grain boundaries. A single iteration of neighbor confidence index (CI) correlation was applied to diffraction spots with CI values below 0.15 to enhance indexing accuracy. The dataset consisted of 81 024 reconstructed grain boundary traces. The five-parameter GBCD space, defined by the angles  $\phi_1$ ,  $\Phi$ ,  $\phi_2$ ,  $\theta$ , and  $\varphi$ , was discretized at a resolution of 10°. The grain boundary distribution analysis was conducted considering the columnar grains (vertical grain boundaries) using a com-

putational code developed by Rohrer et al.<sup>26</sup> The analysis emphasized the distribution of grain boundary planes as a function of varying grain boundary misorientations, providing insights into the grain boundary characteristics of the BCZYYb4411 material. Figure 1 illustrates a schematic of the experimental workflow for the thin film deposition and subsequent characterization.

## 3 | RESULTS

### 3.1 | Structural characterization

XRD analysis of the BCZYYb4411 powder confirms a cubic perovskite structure with space group *Pm-3m* and a lattice parameter of  $a = 4.298 \text{ \AA}$ , as shown in Figure 2A. This lattice parameter aligns well with previously reported values for similar compositions, such as BaCe<sub>0.4</sub>Zr<sub>0.4</sub>Y<sub>0.2</sub>O<sub>3-δ</sub> ( $a = 4.318 \text{ \AA}$ <sup>37</sup> and BaCe<sub>0.7</sub>Zr<sub>0.1</sub>Y<sub>0.1</sub>O<sub>3-δ</sub><sup>38</sup>). The powder includes 1 wt.% NiO as a sintering aid, facilitating the production of a highly dense pellet when sintered at 1450°C (Figure 2B). EDS analysis of the sintered pellet confirms that the atomic percentage ratios of cations Ba:Ce:Zr:Y:Yb are approximately 10:4:4:1:1, closely aligning with the expected stoichiometric composition. The distribution of all constituent elements is uniform as shown in Figure S1.

Figure 2C illustrates the nanocrystalline grains formed in the thin film prepared via PLD. Despite the deposition thickness being in the range of a few tens of nanometers, the grain boundary traces exhibit narrow widths, indicating the columnar nature of the grains. Such nanocrystalline columnar grains are characteristic of PLD-prepared samples.<sup>13,39,40</sup> SAED patterns shown in Figure 2D display ring-type diffraction patterns, suggesting the presence of all crystallographic orientations in the PLD specimen. The SAED patterns are indexed to the same crystal parameters obtained from the XRD data, confirming the stability of the cubic perovskite structure and consistent lattice parameter. This crystal structure (*Pm-3m*,  $a = 4.298$ ) is further utilized to simulate the diffraction patterns for indexing the PED data during orientation microscopy analysis.

### 3.2 | Grain orientation, texture, and grain boundary planes distribution

The orientation distribution map derived from the PED data is presented in Figure 3. Following the cleanup of the raw data, nanocrystalline grains with an average diameter of  $11.9 \pm 3.8 \text{ nm}$  are measured using TSL OIM software. Analysis of grain orientations indicates a preferential texture oriented toward the (0 0 1) crystallographic plane, exhibiting a texture intensity approximately four times greater than the random distribution.

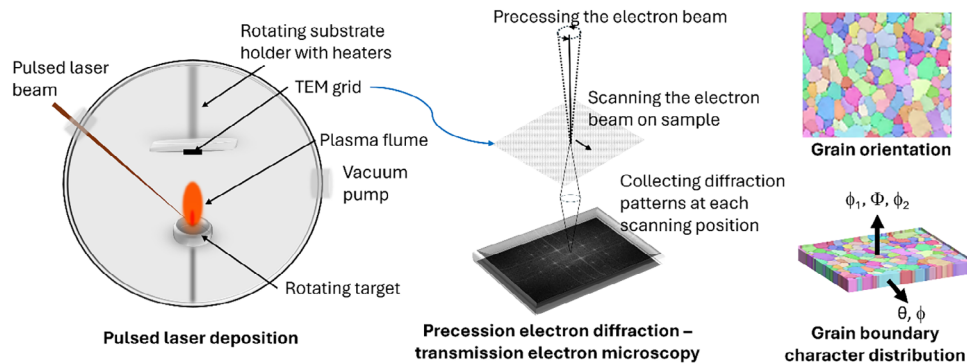


**FIGURE 1** Schematic showing the experimental workflow: BCZYYb4411 thin film deposition on a  $\text{SiO}_2$  transmission electron microscopy (TEM) window grid, orientation mapping using precession electron diffraction (PED)-TEM, and subsequent grain boundary character distribution (GBCD) analysis.

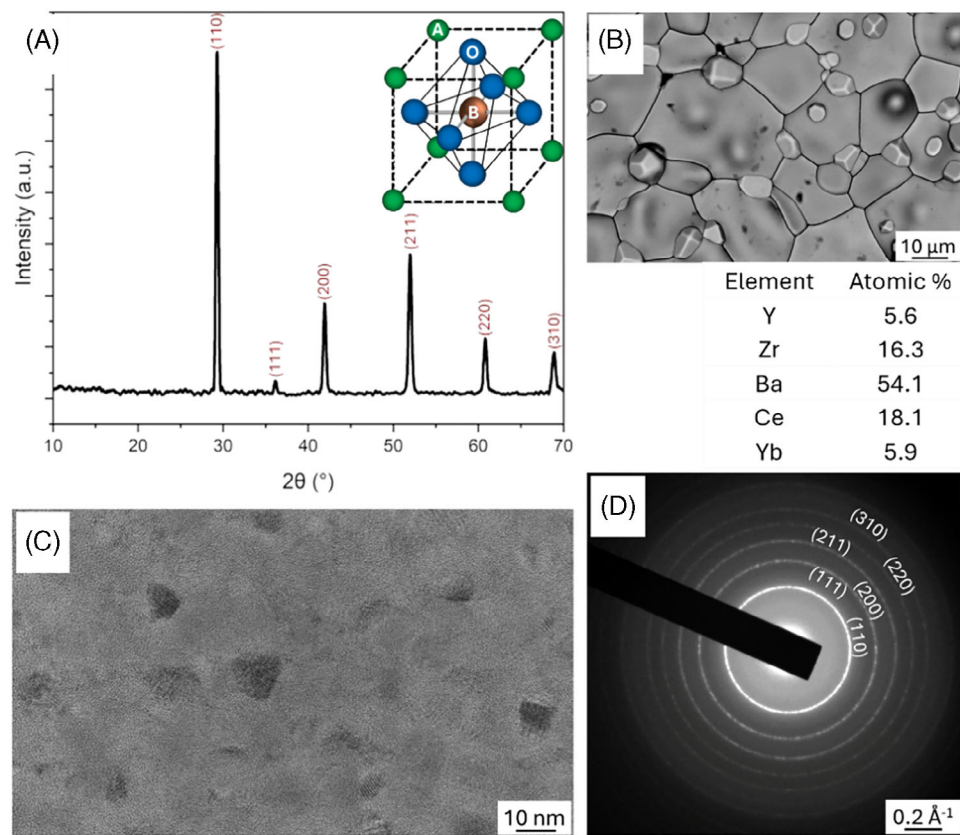


**FIGURE 2** Crystal structure of BCZYYb4411: (A) x-ray diffraction pattern of BCZYYb4411 powder before pulsed laser deposition (PLD) target fabrication, (B) sintered dense PLD target exhibiting the expected chemical composition after sintering at 1450 $^{\circ}\text{C}$ , (C) high-resolution transmission electron microscopy (TEM) image displaying nanocrystalline grains within the PLD-prepared sample, and (D) selected area electron diffraction (SAED) pattern confirming the polycrystalline nature of the grains with a consistent atomic structure.

Figure 4A compares the disorientation angle distribution of BCZYYb4411 samples prepared via PLD with a simulated random distribution for a cubic crystal system. The grain boundary population is higher at disorientation angles below 20 $^{\circ}$ , ~37 $^{\circ}$ , and ~60 $^{\circ}$ , relative to the random

distribution. The length and number fractions of grain boundaries are less than random within the disorientation angle range of 40 $^{\circ}$ –50 $^{\circ}$ .

Figure 4B illustrates the distribution of disorientation axes corresponding to disorientation angles within 10 $^{\circ}$

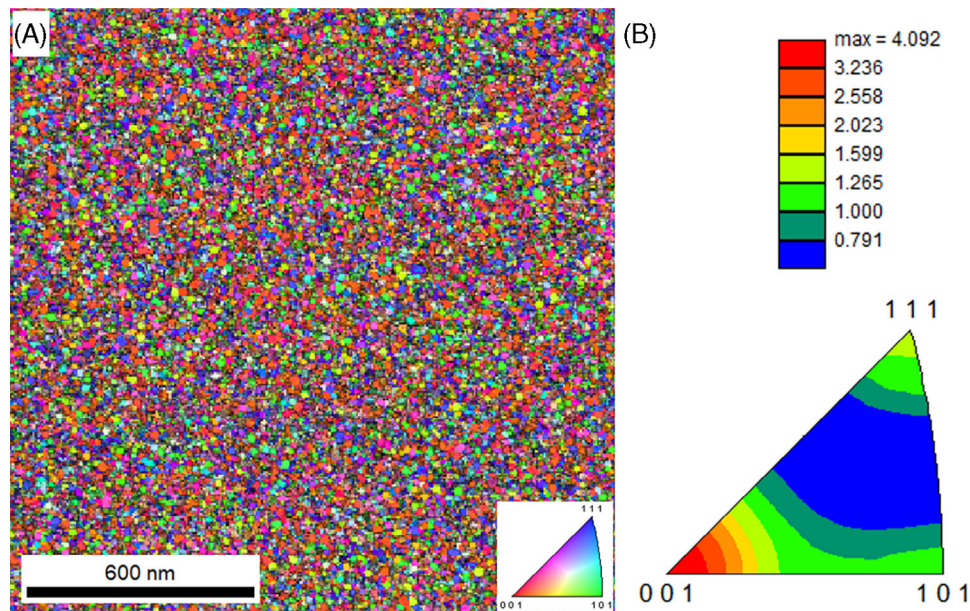


**FIGURE 3** Grain orientation distribution in pulsed laser deposition (PLD)-prepared BCZYYb44I1: (A) precession electron diffraction (PED)-indexed grain orientation distribution map along the normal direction, and (B) grains texture in inverse pole figure along the normal direction. The color scale in (B) represents the multiple of random distribution.

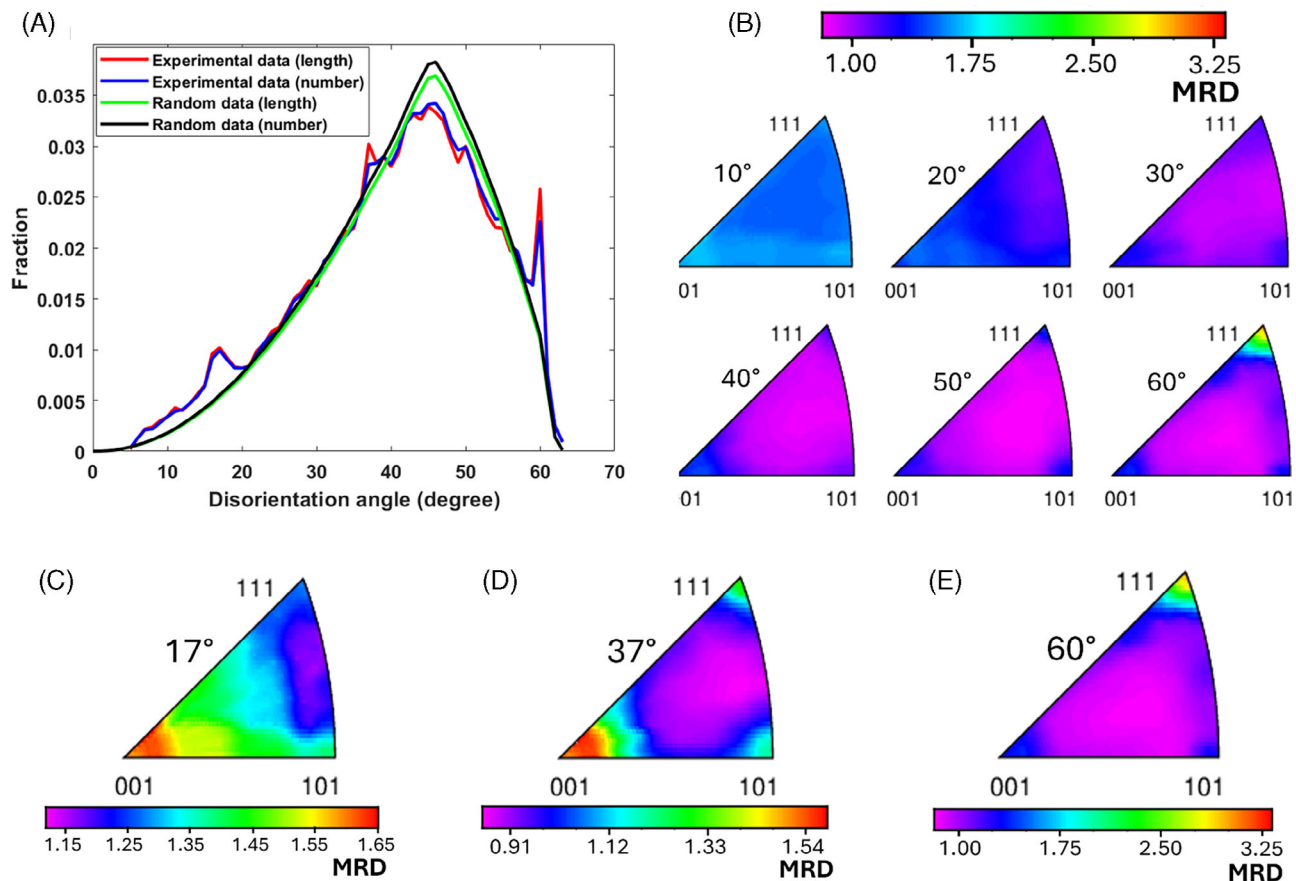


**FIGURE 4** (A) Disorientation angle distribution for pulsed laser deposition (PLD)-prepared BCZYYb44I1 and random grain boundary distribution for cubic systems, (B) distribution of disorientation axis within  $10^\circ$  interval of disorientation angles, and (C–E) distribution of disorientation axes for disorientation angles with populations exceeding the random distribution.

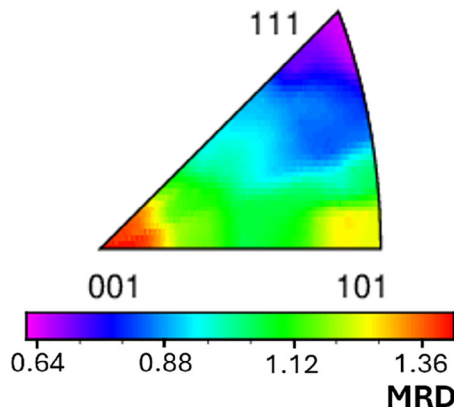


**FIGURE 5** Grain boundary plane distribution in the crystal reference frame for pulsed laser deposition (PLD)-prepared BCZYYb4411.

intervals, each encompassing a  $\pm 5^\circ$  range around the specified angle. The distribution confirms a higher population of grain boundaries at low disorientation angles, with the disorientation axes exhibiting a generally uniform distribution and a slight preferential alignment along the [0 0 1] axis. Specifically, the distributions at disorientation angles of  $17^\circ$ ,  $37^\circ$ , and  $60^\circ$  show that the grain boundary populations are above random distributions. At disorientation angles of  $17^\circ$  and  $37^\circ$ , a higher population of grain boundaries aligns with the [1 0 0] axis, corresponding closely to the special grain boundaries  $\Sigma 25a$  ( $16.3^\circ/[1 0 0]$ ) and  $\Sigma 5$  ( $36.9^\circ/[1 0 0]$ ), respectively. At a disorientation angle of  $60^\circ$ , the increased population is along the [1 1 1] axis, corresponding to the  $\Sigma 3$  special grain boundary.

Figure 5 presents the misorientation-averaged grain boundary plane distribution for the PLD-deposited BCZYYb4411 within the crystal reference frame, confined explicitly to the fundamental zone of orientation space. The distribution reveals anisotropy across the grain boundary planes, exhibiting a maximum deviation of 0.8 MRD. The distribution indicated a preferential alignment of grain boundary plane normals along the [0 0 1] crystallographic direction (1.41 MRD), whereas the [1 1 1] direction exhibits the lowest preference. A comparable trend has been previously reported for  $\text{SrTiO}_3$ , which also possesses a cubic perovskite crystal structure.<sup>32</sup>

GBCD analysis provides a comprehensive dataset wherein each disorientation axis-angle pair corresponds to a distinct grain boundary misorientation. For each disorientation angle, multiple disorientation axes are accessible, facilitating the examination of a broad spectrum of grain boundary misorientations. The GBCD sections can be assessed for these misorientations, pre-

senting the distribution of grain boundary planes through stereographic projections. In the case of PLD-prepared BCZYYb4411, the distributions of disorientation angles (Figure 4A) and disorientation axes (Figure 4B–E) enable the identification of grain boundaries with populations exceeding those expected from random occurrence. Figure 4B illustrates that along the [1 0 0], [1 1 0], and [1 1 1] crystallographic axes, grain boundaries exhibit a frequency exceeding random distribution (>1 MRD) across the entire misorientation angle spectrum. To further investigate the grain boundaries, a five-parameter GBCD analysis was performed for these disorientation axes across  $10^\circ$  intervals throughout the range of disorientation angles.

### 3.2.1 | GBCD sections about the [1 0 0] disorientation axis

The distribution of grain boundary plane normals for misorientation angles within  $10^\circ$  intervals along the [1 0 0] axis is presented in Figure 6. Stereographic projections of geometrically characteristic boundaries, including tilt, twist,  $180^\circ$ -twist, and  $180^\circ$ -tilt configurations corresponding to specific misorientations, are generated using Glowinski's grain boundary toolbox.<sup>41</sup> The analysis reveals a pronounced population density along {1 0 0} twist boundaries, regardless of misorientation angle, consistent with the grain boundary plane distribution shown in Figure 5. Notably, for a misorientation of  $10^\circ/[1 0 0]$ , the highest population density of 5.19 MRD is observed for (1 0 0) twist boundaries (similar observations for  $\Sigma 25a$  ( $16.3^\circ/[1 0 0]$ ) in Figure S2). For the [1 0 0] axis preferred planes, the maximum population along {1 0 0} twist boundaries likely arises because twist boundaries allow both crystals to terminate on {1 0 0} planes.<sup>27</sup> The additional peaks in distribution correspond to  $180^\circ$ -twist grain boundaries.

Specifically, at misorientation of  $10^\circ/[1 0 0]$ , two  $180^\circ$ -tilt boundaries exhibit population densities over three times the random distribution, whereas other  $180^\circ$ -tilt boundaries fall below the random distribution threshold. As the misorientation angle increases, the grain boundary population becomes more uniformly distributed across all  $180^\circ$ -tilt boundaries. At  $40^\circ/[1 0 0]$  misorientation, additional peaks with approximately 2.5 MRD are observed around the poles (1 1 2), corresponding to twist and  $180^\circ$ -tilt boundaries.  $\Sigma 5$  ( $36.9^\circ/[1 0 0]$ ) boundaries, exhibiting the above-random distributions (Figure 4A,D), show similar observations, presented in Figure S2. Such features have not been observed for the annealed  $\text{SrTiO}_3$ , which has a similar crystal symmetry.<sup>32</sup>

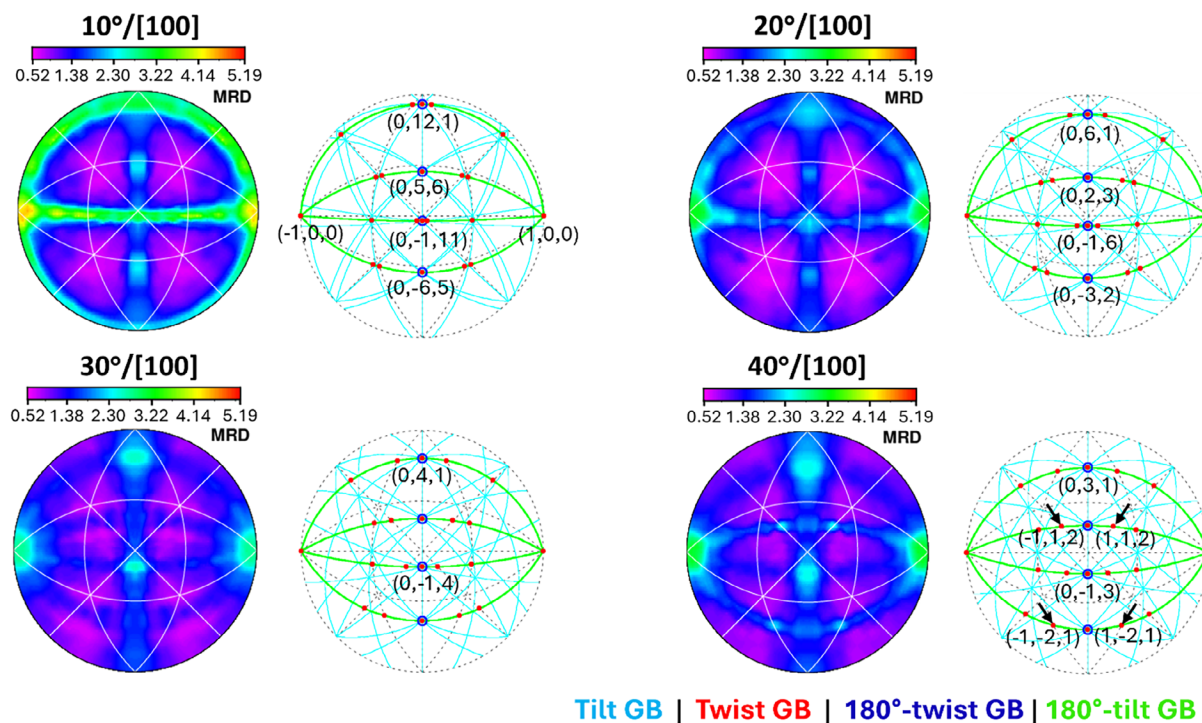


**FIGURE 6** Distribution of grain boundary planes along  $[1\ 0\ 0]$  disorientation axis at various misorientation angles in  $10^\circ$  intervals and corresponding geometrically characteristic grain boundaries.

### 3.2.2 | GBCD sections about the $[1\ 1\ 0]$ disorientation axis

The distribution of grain boundary plane normals for various misorientation angles about the  $[1\ 1\ 0]$  axis is illustrated in Figure 7. Consistent with observations for misorientations about the  $[1\ 0\ 0]$  axis, the grain boundary population density remains higher along  $\{1\ 1\ 0\}$  twist boundaries, with an average exceeding 4 MRD across all misorientation angles. Additionally, an arc of increased population density ( $>3$  MRD) is distinctly observed for all misorientation angles, corresponding to  $180^\circ$ -tilt boundaries, as illustrated in the geometrically characteristic grain boundaries figures.

At a misorientation of  $10^\circ/[1\ 1\ 0]$ , multiple additional peaks are identified for twist grain boundaries about the poles  $(0\ 17\ 1)$  and  $(0\ 1\ 1)$ , as well as for  $180^\circ$ -twist grain boundaries about the poles  $(-8\ 8\ 1)$  and  $(1\ -1\ 21)$ . Among these twist boundaries, the grain boundary population remains considerably higher ( $>4$  MRD) along the arc associated with  $180^\circ$ -tilt grain boundaries. This trend is consistent across all examined misorientations about the  $[1\ 1\ 0]$  axis. The maximum population density with 6.91 MRD is observed at a misorientation of  $50^\circ/[1\ 1\ 0]$  ( $\Sigma 11$ -special grain boundary), corresponding to the twist and  $180^\circ$ -tilt grain boundaries about the poles  $(-1\ 2\ 1)$  and  $(-2\ 1\ 1)$ .

### 3.2.3 | GBCD sections about the $[1\ 1\ 1]$ disorientation axis

The distribution of grain boundary plane normals about the  $[1\ 1\ 1]$  axis for specific misorientation angles is presented in Figure 8. At a misorientation of  $10^\circ/[1\ 1\ 1]$ , the  $180^\circ$ -twist grain boundaries exhibit a significant population density, reaching approximately 4.1 MRD. Except for the  $\{1\ 1\ 1\}$  twist boundaries, all twist grain boundaries show at least twice the population density compared to the random distribution. Notably, the population of  $\{1\ 1\ 1\}$  twist boundaries rises with increasing misorientation angle. However, these boundaries are not the dominant ones for all misorientation angles, unlike the dominance observed in  $\{1\ 0\ 0\}$  and  $\{1\ 1\ 0\}$  twist boundaries along the  $[1\ 0\ 0]$  and  $[1\ 1\ 0]$  disorientation axes, respectively. The misorientation-averaged grain boundary plane distribution (Figure 5) reveals a population density lower than the random distribution for grain boundary plane normals along  $[1\ 1\ 1]$ .

For misorientation angles between  $20^\circ$  and  $40^\circ$ , most grain boundaries exhibit a distribution close to random, except for certain twist grain boundaries. The distributions for the  $20^\circ$  and  $30^\circ$  misorientation angles are provided in Figure S5. At higher misorientation angles of  $50^\circ$  and  $60^\circ$ , the population density ( $>7$  MRD) becomes concentrated along the  $\{1\ 1\ 1\}$  twist axis and around the twist

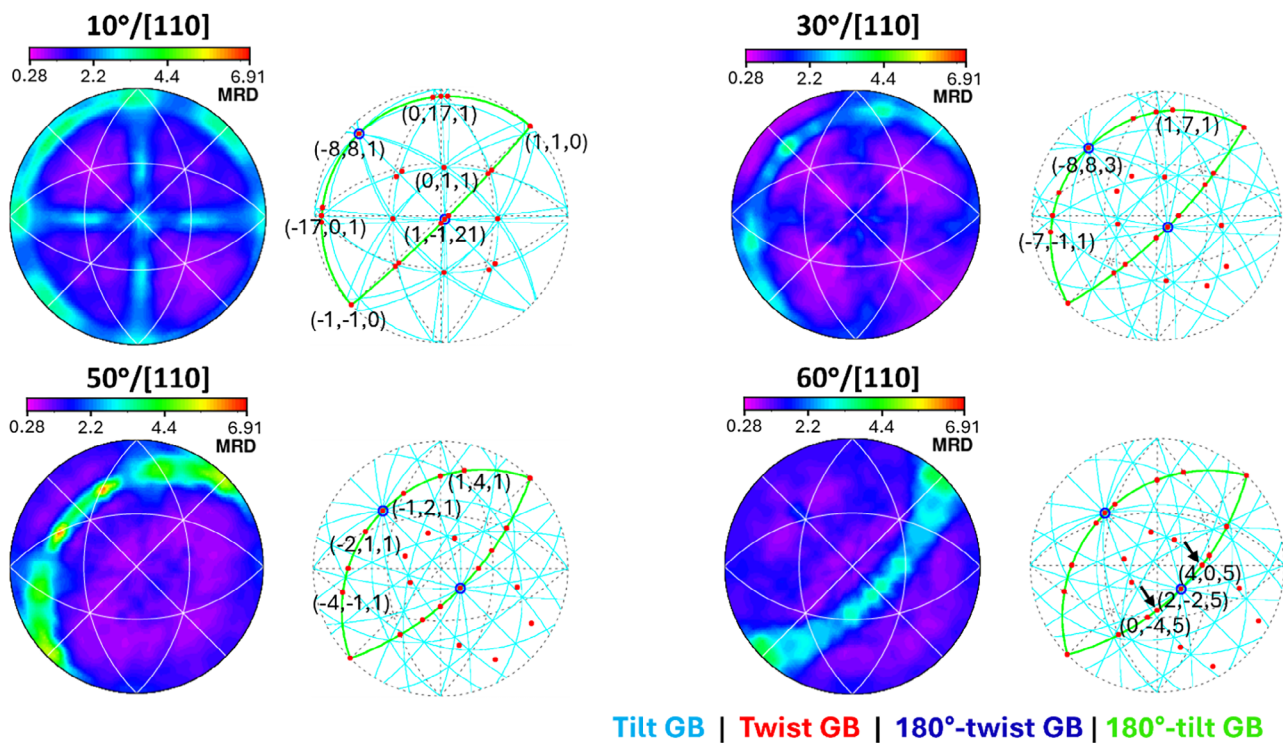


**FIGURE 7** Distribution of grain boundary planes along  $[1\bar{1}0]$  disorientation axis at various misorientation angles and corresponding geometrically characteristic grain boundaries.

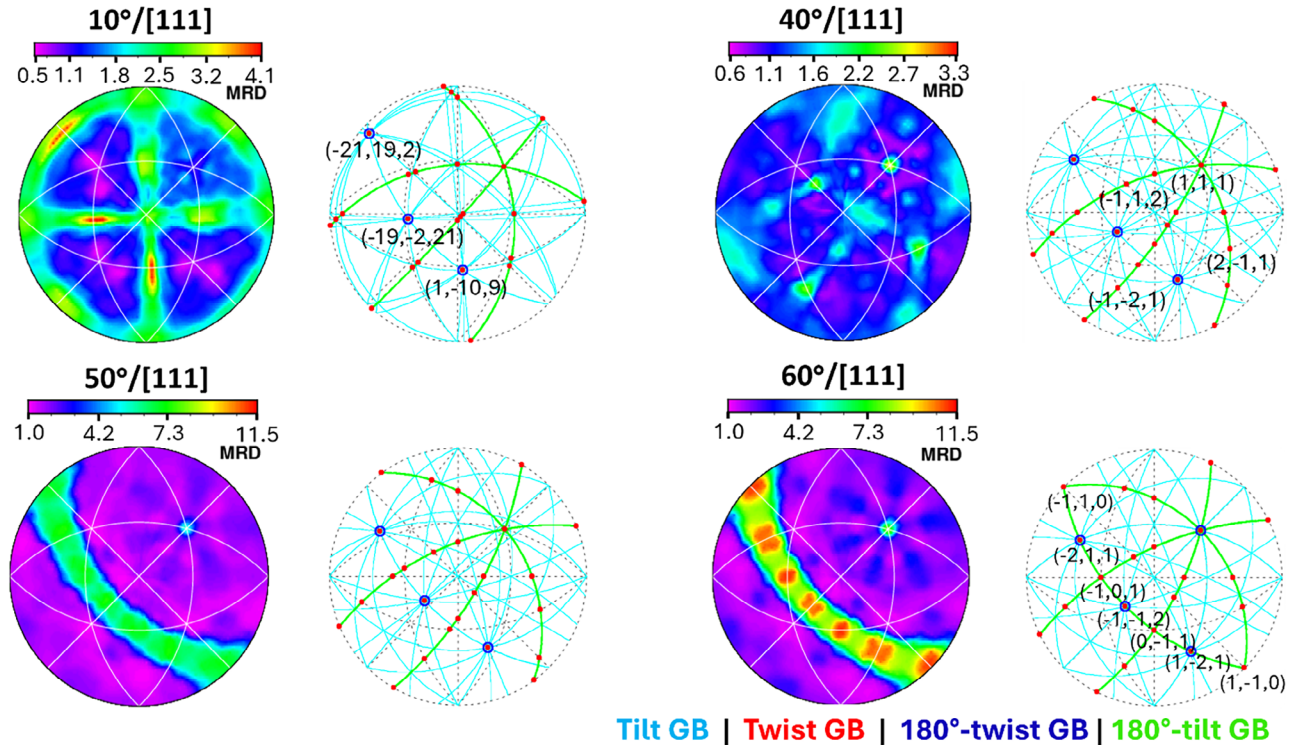


**FIGURE 8** Distribution of grain boundary planes along  $[1\bar{1}\bar{1}]$  disorientation axis at various misorientation angles and corresponding geometrically characteristic grain boundaries.

TABLE 1 A summary of the highest grain boundary population about the special grain boundaries.

Special grain boundary	Misorientation angle/axis	Highest MRD	Corresponding pole	Characteristic grain boundary type
$\Sigma 1$	$5^\circ/[1\ 1\ 1]$	4.14	(−1 1 0), (−1 0 1), (0 −1 1)	$180^\circ$ -twist
$\Sigma 7$	$38.2^\circ/[1\ 1\ 1]$	4.56	(1 1 1)	Twist, $180^\circ$ -tilt
$\Sigma 9$	$38.9^\circ/[1\ 1\ 0]$	3.86	(1 5 1), (−5 −1 1)	Twist, $180^\circ$ -tilt
$\Sigma 13a$	$22.6^\circ/[1\ 0\ 0]$	3.23	(1 0 0), (−1 0 0)	Twist, $180^\circ$ -tilt
$\Sigma 13b$	$27.8^\circ/[1\ 1\ 1]$	2.29	(1 −1 8)	Twist, $180^\circ$ -tilt
$\Sigma 15$	$48.2^\circ/[2\ 1\ 0]$	1.82	(−1 5 −2 2)	Twist, $180^\circ$ -tilt
$\Sigma 17a$	$28.1^\circ/[1\ 0\ 0]$	2.68	(1 0 0), (−1 0 0)	Twist, $180^\circ$ -tilt
$\Sigma 17b$	$61.9^\circ/[2\ 2\ 1]$	5.57	(0 −1 1)	Twist, $180^\circ$ -tilt
$\Sigma 19a$	$26.5^\circ/[1\ 1\ 0]$	4.33	(2 −2 13)	$180^\circ$ -twist
$\Sigma 19b$	$46.8^\circ/[1\ 1\ 1]$	2.01	(1 1 1), (−3 3 7)	Twist, $180^\circ$ -tilt
$\Sigma 21a$	$21.8^\circ/[1\ 1\ 1]$	2.25	(−4 0 1)	Twist, $180^\circ$ -tilt

boundaries on an arc of  $180^\circ$ -tilt boundaries perpendicular to pole (1 1 1). At  $60^\circ/[1\ 1\ 1]$  ( $\Sigma 3$ -special grain boundary), the maximum population density, approximately 11 MRD, is associated with twist grain boundaries around the poles (−1 1 0), (−1 0 1), (0 1 1), and (1 0 −1), and  $180^\circ$ -twist grain boundaries around the poles (−2 1 1), (−1 −1 2), and (1 −2 1). These boundaries represent either the conjunction of two  $180^\circ$ -tilt boundaries or a conjunction of multiple tilt boundaries.

### 3.2.4 | GBCD sections at the special grain boundaries

The special grain boundaries  $\Sigma 3$  ( $60^\circ/[1\ 1\ 1]$ ) and  $\Sigma 11$  ( $50.5^\circ/[1\ 1\ 0]$ ) exhibit significantly higher population densities of 11.5 and 6.91 MRD, respectively, for specific combinations of twist and  $180^\circ$ -tilt grain boundaries. To further elucidate the grain boundary plane distribution, GBCD sections for the special boundaries are analyzed. The summarized data is presented in Table 1, with detailed plots in Figure S6. Notably, the  $\Sigma 17(b)$  ( $61.9^\circ/[2\ 2\ 1]$ ) boundary exhibits a relatively high population density of 5.57 MRD, associated with the pole (0 −1 1). This twist boundary is attributed to the intersection of two distinct  $180^\circ$ -tilt grain boundaries, as detailed in characteristic grain boundaries plot of Figure S6. Furthermore, in the axis-angle plot (Figure 4E), a  $60^\circ$  misorientation reveals a slight population enhancement above the random distribution for the [2 1 2] axis.

## 3.3 | Discussion and motivation

This study highlights GBCD as a tool for characterizing the complex grain boundary landscape in PCC

electrolyte materials and identifying the most frequent boundaries for further analysis. Our findings reveal that grain boundary planes terminating along the [1 0 0] direction are more prevalent than others. Within the misorientation space for the [1 0 0] axis, {1 0 0} twist boundaries consistently exhibit a higher population density. Additionally, for misorientations around [1 1 0] and [1 1 1], certain twist grain boundaries on the curve of  $180^\circ$ -tilt boundaries demonstrate high population density. The observed texture along [1 0 0] orientation and the nonuniform distribution of grain boundary plane normals recommend that tailoring the PLD parameters and/or varying the concentration of sintering aids or dopants could be an effective strategy to modify grain boundary distribution.

Grain boundaries are crucial in determining the overall proton conductivity of PCC electrolytes.

Their disordered atomic arrangement results in higher energy than the bulk crystal lattice. This elevated energy facilitates the preferential segregation of impurities, dopants, and sintering aids at the grain boundaries, leading to modifications in grain boundary energy. Such alterations can be one of the reasons for an anisotropy in the grain boundary distribution.

The GBCD analysis in PCC electrolytes establishes a foundation for investigating critical properties, including proton migration energy barriers across specific grain boundary configurations, the segregation behavior of dopants and sintering aids, and the impact of such segregation on grain boundary energy. This approach seeks to enhance proton conductivity and chemical stability in PCC electrolytes. Computational simulations could further explore the correlation between grain boundary distribution and proton migration energy barriers to guide performance optimization.

Although this study provides valuable insights into the mesoscale distribution of grain boundaries, the direct relationship between specific grain boundary characteristics and proton conductivity remains complex. This complexity arises from the intricate nature of grain boundary interactions at the atomic scale and the limited computational data available for the multicomponent PCC electrolyte system. Advancing our understanding requires further research, integrating atomistic simulations with advanced characterization techniques, to investigate the influence of frequently observed grain boundaries on proton transport properties. This multidisciplinary approach holds considerable potential for developing next-generation PCC electrolytes with enhanced performance, offering greater efficiency and durability for proton-conducting electrochemical cells.

## 4 | CONCLUSION

In this study, nanocrystalline grains are synthesized by depositing a thin film of the PCC electrolyte material  $\text{BaCe}_{0.4}\text{Zr}_{0.4}\text{Y}_{0.1}\text{Yb}_{0.1}\text{O}_{3-\delta}$  using PLD. The grain orientation dataset is obtained through precession-based electron diffraction patterns, which are subsequently indexed to determine the grain orientations. The five-parameter GBCD is assessed to identify the predominant grain boundaries in this PCC electrolyte material. The distribution of grain boundary plane normals is investigated by performing GBCD sections along the high-population misorientation axes across the entire range of misorientation angles.

Key findings are as follows:

- The PLD-prepared BCZYYb4411 thin film exhibits nanocrystalline columnar grains with an average size of  $11.9 \pm 3.8$  nm. Grain orientation along the normal direction shows a texture intensity of four MRD toward the (1 0 0) orientation.
- The grain boundary distribution shows a preference for disorientation angles less than  $20^\circ$ , as well as around  $37^\circ$  and  $60^\circ$ . The population densities are considerably higher along the [1 0 0], [1 1 0], and [1 1 1] disorientation axes. The grain boundary plane normals distributions in a crystal reference frame show a preference along the [0 0 1] crystallographic direction.
- The GBCD plots reveal an asymmetric distribution across different misorientation angles. The majority of high-density boundaries corresponded to twist and  $180^\circ$ -tilt boundary configurations.
- $\Sigma 3$  boundaries ( $60^\circ/[1\ 1\ 1]$ ) exhibit the highest population density of 11.5 MRD, corresponding to twist and  $180^\circ$ -tilt grain boundaries perpendicular to the pole

(1 1 1).  $\Sigma 11$  boundaries ( $50.5^\circ/[1\ 1\ 0]$ ) show the second-highest population density of 6.91 MRD, associated with twist and  $180^\circ$ -tilt grain boundaries about the poles ( $-1\ 2\ 1$ ) and ( $-2\ 1\ 1$ ).

## ACKNOWLEDGMENTS

This research was supported by a grant from the Research Council of the University of Oklahoma, and Samual Roberts Noble Microscopy Laboratory at the University of Oklahoma. F. Liu and D. Ding would like to thank the support of the HydroGEN Advanced Water Splitting Materials Consortium, established as part of the Energy Materials Network under the U.S. Department of Energy (USDOE); the Office of Energy Efficiency and Renewable Energy (EERE); the Hydrogen and Fuel Cell Technologies Office (HFTO) under DOE Idaho Operations Office under contract no. DE-AC07-05ID14517.

## CONFLICT OF INTEREST STATEMENT

The authors declare no conflicts of interest.

## DECLARATION OF GENERATIVE AI AND AI-ASSISTED TECHNOLOGIES IN THE WRITING PROCESS

During the preparation of this work, the authors used ChatGPT to improve the readability and language of the manuscript. After using this tool, the authors reviewed and edited the content as needed and took full responsibility for the content of the published article.

## ORCID

Sooraj Patel  <https://orcid.org/0000-0002-5639-6214>

## REFERENCES

- Choi M, Paik J, Kim D, Woo D, Lee J, Kim SJ, et al. Exceptionally high performance of protonic ceramic fuel cells with stoichiometric electrolytes. *Energy Environ Sci.* 2021;14(12): 6476–83.
- An H, Lee H-W, Kim B-K, Son J-W, Yoon KJ, Kim H, et al. A  $5 \times 5 \text{ cm}^2$  protonic ceramic fuel cell with a power density of  $1.3 \text{ W cm}^{-2}$  at  $600^\circ\text{C}$ . *Nature Energy.* 2018;3(10):870–75.
- Duan C, Kee RJ, Zhu H, Karakaya C, Chen Y, Ricote S, et al. Highly durable, coking and sulfur tolerant, fuel-flexible protonic ceramic fuel cells. *Nature.* 2018;557(7704):217–22.
- Liu F, Deng H, Diercks D, Kumar P, Jabbar MHA, Gumeci C, et al. Lowering the operating temperature of protonic ceramic electrochemical cells to  $<450^\circ\text{C}$ . *Nature Energy.* 2023;8(10):1145–57.
- Choi SM, An H, Yoon KJ, Kim B-K, Lee H-W, Son J-W, et al. Electrochemical analysis of high-performance protonic ceramic fuel cells based on a columnar-structured thin electrolyte. *Appl Energy.* 2019;233:29–36.
- Bae K, Kim DH, Choi HJ, Son JW, Shim JH. High-performance protonic ceramic fuel cells with  $1 \mu\text{m}$  Thick Y:  $\text{Ba}(\text{Ce}, \text{Zr})\text{O}_3$  electrolytes. *Adv Energy Mater.* 2018;8(25):1801315.

7. Le LQ, Hernandez CH, Rodriguez MH, Zhu L, Duan C, Ding H, et al. Proton-conducting ceramic fuel cells: scale up and stack integration. *J Power Sources*. 2021;482:228868.
8. Zhang L, Hu S, Cao Z, Pang B, Wang J, Zhang P, et al. Repeatable preparation of defect-free electrolyte membranes for proton-conducting fuel cells. *J Membr Sci*. 2022;656:120642.
9. Yang L, Wang S, Blinn K, Liu M, Liu Z, Cheng Z, et al. Enhanced sulfur and coking tolerance of a mixed ion conductor for SOFCs:  $\text{BaZr}_{0.1}\text{Ce}_{0.7}\text{Y}_{0.2-x}\text{Yb}_x\text{O}_{3-\delta}$ . *Science*. 2009;326(5949):126–29.
10. Tang M, Niu Y, Muhammad W, Muhammad S, Zhong Z, Muhammad S, et al. Advances in solid oxide fuel cell electrolyte fabrication by pulsed laser deposition. *Int J Hydrogen Energy*. 2024;50:618–32.
11. Niwa E, Kluczny M, Kim HY, Song JT, Watanabe M, Takagaki A, et al. Proton conductivity in Yb-doped  $\text{BaZrO}_3$ -based thin film prepared by pulsed laser deposition. *Solid State Ionics*. 2023;396:116240.
12. Zheng H, Han F, Sata N, Riegraf M, Dayaghi AM, Norby T, et al. Metal supported proton conducting ceramic cell with thin film electrolyte for electrolysis application. *ECS Trans*. 2021;103(1):693.
13. Bae K, Jang DY, Choi HJ, Kim D, Hong J, Kim B-K, et al. Demonstrating the potential of yttrium-doped barium zirconate electrolyte for high-performance fuel cells. *Nat Commun*. 2017;8(1):14553.
14. Patel S, Liu F, Ding H, Duan C, Ghamarian I. On proton conduction mechanism for electrolyte materials in solid oxide fuel cells. *Int J Hydrogen Energy*. 2024;72: 1236–48.
15. Yamazaki Y, Hernandez-Sanchez R, Haile SM. High total proton conductivity in large-grained yttrium-doped barium zirconate. *Chem Mater*. 2009;21(13):2755–62.
16. Shirpour M, Merkle R, Lin C, Maier J. Nonlinear electrical grain boundary properties in proton conducting  $\text{Y}-\text{BaZrO}_3$  supporting the space charge depletion model. *Phys Chem Chem Phys*. 2012;14(2):730–40.
17. Shirpour M, Merkle R, Maier J. Space charge depletion in grain boundaries of  $\text{BaZrO}_3$  proton conductors. *Solid State Ionics*. 2012;225:304–7.
18. Iguchi F, Chen C-T, Yugami H, Kim S. Direct evidence of potential barriers at grain boundaries in Y-doped  $\text{BaZrO}_3$  from dc-bias dependence measurements. *J Mater Chem*. 2011;21(41):16517–23.
19. Watanabe T. The importance of grain boundary character distribution (GBCD) to recrystallization, grain growth and texture. *Scr Metall Mater*. 1992;27(11):1497–502.
20. Feng W, Yang S, Yan Y. Dependence of grain boundary character distribution on the initial grain size of 304 austenitic stainless steel. *Philos Mag*. 2017;97(13):1057–70.
21. Song S-H, Zhao Y, Cui Y, Sun J, Si H, Li J-Q. Effect of grain boundary character distribution and grain boundary phosphorus segregation on the brittleness of an interstitial-free steel. *Mater Lett*. 2016;182:328–31.
22. Papillon F, Rohrer GS, Wynblatt P. Effect of segregating impurities on the grain-boundary character distribution of magnesium oxide. *J Am Ceram Soc*. 2009;92(12):3044–51.
23. Barr CM, Foiles SM, Alkayyali M, Mahmood Y, Price PM, Adams DP, et al. The role of grain boundary character in solute segregation and thermal stability of nanocrystalline Pt–Au. *Nanoscale*. 2021;13(6):3552–63.
24. Sutton AP, Balluffi RW. Interfaces in crystalline materials. England: Clarendon Press; 1995.
25. Faryna M, Glowinski K. Five dimensional grain boundary distribution for yttria stabilized zirconia based on experimentally determined macroscopic boundary parameters. *Acta Mater*. 2022;226:117606.
26. Rohrer GS, Saylor DM, El Dasher B, Adams BL, Rollett AD, Wynblatt P. The distribution of internal interfaces in polycrystals. *Int J Mater Res*. 2021;95(4):197–214.
27. Saylor DM, Morawiec A, Rohrer GS. Distribution of grain boundaries in magnesia as a function of five macroscopic parameters. *Acta Mater*. 2003;51(13):3663–74.
28. Saylor DM, El Dasher BS, Rollett AD, Rohrer GS. Distribution of grain boundaries in aluminum as a function of five macroscopic parameters. *Acta Mater*. 2004;52(12):3649–55.
29. Ghamarian I, Samimi P, Rohrer G, Collins PC. Determination of the five parameter grain boundary character distribution of nanocrystalline alpha-zirconium thin films using transmission electron microscopy. *Acta Mater*. 2017;130:164–76.
30. Kelly MN, Glowinski K, Nuhfer NT, Rohrer GS. The five parameter grain boundary character distribution of  $\alpha$ -Ti determined from three-dimensional orientation data. *Acta Mater*. 2016;111:22–30.
31. Miller HM, Saylor D, El Dasher BS, Rollett AD, Rohrer GS. Crystallographic distribution of internal interfaces in spinel polycrystals. *Mater Sci Forum*. 2004;467:783–88.
32. Saylor DM, El Dasher B, Sano T, Rohrer GS. Distribution of grain boundaries in  $\text{SrTiO}_3$  as a function of five macroscopic parameters. *J Am Ceram Soc*. 2004;87(4):670–76.
33. Dillon SJ, Shen YF, Rohrer GS. Grain boundary energies in yttria-stabilized zirconia. *J Am Ceram Soc*. 2022;105(4):2925–31.
34. Ebert JN, Jennings D, Schäfer L-A, Sebold D, Rheinheimer W. Bulk and grain boundary conductivity in doped  $\text{BaZrO}_3$ : bulk contribution dominates at operating temperatures. *Scr Mater*. 2024;241:115852.
35. Kindelmann M, Escolastico S, Almar L, Vayyala A, Jennings D, Deibert W, et al. Highly conductive grain boundaries in cold-sintered barium zirconate-based proton conductors. *J Mater Chem A*. 2024;12(7):3977–88.
36. Ghamarian I, Samimi P, Liu Y, Poorganji B, Vasudevan VK, Collins PC. Characterizing the nano-structure and defect structure of nano-scaled non-ferrous structural alloys. *Mater Charact*. 2016;113:222–31.
37. Basbus JF, Arce MD, Napolitano FR, Troiani HE, Alonso JA, Saleta ME, et al. Revisiting the crystal structure of  $\text{BaCe}_{0.4}\text{Zr}_{0.4}\text{Y}_{0.2}\text{O}_{3-\delta}$  proton conducting perovskite and its correlation with transport properties. *ACS Appl Energy Mater*. 2020;3(3):2881–92.
38. Chen L, Jing J, Lun P, Zhang P, Zheng Z, Wang H, et al.  $\text{Ba}_{0.9}\text{Co}_{0.7}\text{Fe}_{0.2}\text{Nb}_{0.1}\text{O}_{3-\delta}$  perovskite as promising cathode material for proton ceramic fuel cell. *Int J Hydrogen Energy*. 2023;48(100):39981–88.
39. Xu M, Yu J, Song Y, Ran R, Wang W, Shao Z. Advances in ceramic thin films fabricated by pulsed laser deposition for intermediate-temperature solid oxide fuel cells. *Energy Fuels*. 2020;34(9):10568–82.
40. Guo H, Vahidi H, Kang H, Shah S, Xu M, Aoki T, et al. Tuning grain boundary cation segregation with oxygen deficiency and

- atomic structure in a perovskite compositionally complex oxide thin film. *Appl Phys Lett.* 2024;124(17):171605.
41. Glowinski K, Morawiec A. A toolbox for geometric grain boundary characterization. Proceedings of the 1st International Conference on 3D Materials Science, The Minerals, Metals & Materials Society, 2012; Cham: Springer; 2012. p. 119–24.

**How to cite this article:** Patel S, Goswami S, Paul P, Liu F, Zheng S, Sabisch JE, et al. Orientation microscopy-assisted grain boundary analysis for protonic ceramic cell electrolytes. *J Am Ceram Soc.* 2025;108:e20371. <https://doi.org/10.1111/jace.20371>

## SUPPORTING INFORMATION

Additional supporting information can be found online in the Supporting Information section at the end of this article.